www.czasopisma.pan.pl PAN www.journals.pan.pl
Opto-Electronics Review 27 (2019) 18–24

Contents lists available at ScienceDirect

Opto-Electronics Review

journal homepage: http://www.journals.elsevier.com/opto-electronics review

Tunable passively Q-switched ytterbium-doped fiber laser using $MoWS_2$/rGO nanocomposite saturable absorber

J. Mohanraj [a], V. Velmurugan [b], S. Sivabalan [c,*]

[a] Department of Electronics and Communication Engineering, Vel Tech Rangarajan Dr. Sagunthala R&D Institute of Science and Technology, Avadi, Chennai 600062, TN, India
[b] Centre for Nanotechnology Research, Vellore Institute of Technology, Vellore, 632 014, India
[c] School of Electrical Engineering, Vellore Institute of Technology, Vellore, 632 014, India

ARTICLE INFO

Article history:
Received 21 August 2018
Received in revised form
10 November 2018
Accepted 19 November 2018
Available online 22 January 2019

Keywords:
Transition metal dichalcogenides
Q-switched fiber laser
Molybdenum
Tungsten disulfide
Saturable absorber

ABSTRACT

We demonstrated a tunable Q-switched ytterbium-doped fiber laser (YDFL) using $MoWS_2$/rGO nanocomposite as passive saturable absorber. Further, the $Mo_{1-x}W_xS_2$/rGO nanosheets, with x proportion of 0.2, are synthesized using hydrothermal exfoliation technique. The proposed nanocomposite-PVA based thin film is fabricated by mixing the $MoWS_2$/rGO nanosheets with polyvinyl alcohol (PVA). The fabricated thin film is sandwiched between two fiber ferrules to realize the proposed saturable absorber (SA). Further, the proposed $MoWS_2$/rGO-PVA based thin film SA exhibits a fast relaxation time and a high damage threshold which are suitable to realize a Q-switched pulsed laser with a tunable wavelength range of 10 nm that extends from 1028 nm to 1038 nm. For the highest pump power of 267.4 mW, the generated Q-switched pulses exhibit a narrow pulse width of 1.22 μs, the pulse repetition rate of 90.4 kHz, the highest pulse energy of 2.13 nJ and its corresponding average power of 0.193 mW. To the best of author's knowledge, this is the first realization of a tunable Q-switching fiber laser in a 1 μm wavelength using $MoWS_2$/rGO nanocomposite saturable absorber.

1. Introduction

Over the last decade, the tunable passively Q-switched ytterbium doped fiber lasers (YDFLs) are extensively investigated in potential applications such as optical communication, biomedical imaging, metrology and material processing [1–4]. The recent exploration of 2D materials pays the way for tremendous improvement in the development of all fiber tunable YDFLs [5]. Among 2D materials, graphene is highly preferred for its unique characteristics such as broadband absorption [6], high thermal stability [7], and fast nonlinear optical response [8]. On the other hand, it holds zero bandgap and weak modulation depth which limit performance of a graphene based saturable absorber (SA) [9]. Therefore, the focus shifted to other 2D materials such as black phosphorus [10], transition metal dichalcogenides (TMDs) [11–14], and topological insulators [15,16]. Among these, TMDs are suitable for the fabrication of a saturable absorber due to its distinct characteristics such as ultrafast carrier dynamics, strong photoluminescence and good optical absorption [17–19].

Recently, alloying different TMD materials are quite interesting for the following facts such as high thermal stability, enhanced optical absorption, and an improved layer-dependent characteristics [20,21]. Currently, advances in chemical synthesis process initiated the exploration of alloying TMDs for various applications such as development of field effect transistors [22], hydrogen evolution catalysis [23], and photocurrent generation [24]. Potential characteristics of alloyed TMD are then utilized to develop a saturable absorber with an enhanced performance for the laser pulse generation. Very recently, $Mo_{1-x}W_xS_2$ with the x proportion of 0.2 is synthesized for the application of hydrogen evolution performance [25]. This newly fabricated TMD material holds various significant advantages over the current TMDs such as wide tunable bandgap and improved structural properties which help in the development of high performance SA for the ultra-short pulse generation. Further, these alloyed TMD nanosheets can be easily stacked with other materials like graphene, carbon nantubes for the enhancement of SA properties [26,27]. From the literature, it is found that the stacking of reduced-graphene oxide (rGO) with the alloyed TMDs exposes more active edge sites which, in turn, enhance the tunable property of a bandgap and improves the photo-responses [28,29].

In this work, the SA made up of rGO-$Mo_{(1-x)}W_xS_2$ nanocomposite has been fabricated and incorporated into an YDFL cavity operating at 1 μm wavelength. An all-fiber tunable Q-switching

* Corresponding author.
E-mail address: ssivabalan@vit.ac.in (S. Sivabalan).

https://doi.org/10.1016/j.opelre.2018.11.001
1230-3402/

YDFL based on $MoWS_2$@rGO/PVA-SA, gen- erates the stable pulses with a centre wavelength of 1036.88 nm for a FWHM of ~ 2.86 nm and the tunable operating range from 1028 nm to 1038 nm. For the input pump power ranges from 146.7 mW to 267.4 mW, Q-switched pulses exhibit the pulse width from 2.69 μs to 1.22 μs, the pulse repetition rate from 50.70 kHz to 90.84 kHz, the output average power from 0.09 mW to 0.193 mW, and the pulse energy from 1.77 nJ to 2.13 nJ, respectively. According to the authors' knowledge, this is the first realization of a tunable Q-switching YDFL using $MoWS_2$/rGO nanocomposite saturable absorber.

2. Material preparation and characterization

2.1. Synthesis of few-layer $MoWS_2$ nanosheets

2.1.1. Reagents

Sodium molybdenum oxide dihydrate ($Na_2MoO_4.2H_2O$), sodium tungstate dihydrate ($Na_2WO_4.2H_2O$), thiocarbamide (CH_4N_2S), oxalic acid ($H_2C_2O_4$), and hydroxylamine hydrochloride (H_3NoHcl).

2.1.2. Preparation of few-layer $MoWS_2$ nanosheets

The few-layer molybdenum tungsten disulfide ($MoWS_2$) nanosheets were exfoliated using a hydrothermal exfoliation technique [25]. Initially, the mixture of 900 mg of $Na_2MoO_4.2H_2O$ and 70 mg of $Na_2WO_4.2H_2O$ bulk powder (≥ 99%, Sigma-Aldrich) were dissolved in a 60 ml of pure water. Then, 320 mg of $H_2C_2O_4$, 240 mg of H_3NoHcl and 340 mg of CH_4N_2S were mixed in the above solution with stirring process for 50 min. Further, the resultant dispersed solution was transfered into a 50 ml teflon-coated autoclave and kept in a hot furnace at the temperature of 240 °C for 36 h. After the heating process, the resultant solution was collected and purified using the mixture of ethanol and water to filter the impurities. Subsequently, the resultant product was replaced into the petri dish and heated in the hot air oven at the temperature of 70 °C for 16 h. After the completion of wet process, the synthesized sample was gathered and grained. Further, it was dispersed with the suitable solvent N-methyl pyrrolidine (NMP) with a concentration of 15 mg ml^{-1}. Next, the sonication process was executed using bath sonicator for 6 h to remove the residues. The final dispersed solution was the few-layer $Mo_{(1-x)}W_xS_2$ nanosheets which was pale green in colour for the x composition of 0.2.

2.2. Synthesis of GO and reduced-GO (r-GO)

2.2.1. Reagents

Flake graphite powder, 30% Hydrogen peroxide (H_2O_2), Potassium per-manganate ($KMnO_4$), Hydrochloric acid (H_2SO_4) and dilute Hydrochloric acid (HCl).

2.2.2. Oxidation of graphite

Graphene oxide was synthesized from flake graphite by implementing the modified Hummers techniques [30,31]. In a general procedure, 150 mg of flake graphite powder was added with 30 ml of H_2SO_4 and then the dispersed solution was stirred vigorously with a controlled temperature of 5 °C using ice bath. Further, the 8 g of $KMnO_4$ was slowly dispersed into the resultant product and then the solution was shifted to water bath which maintains a temperature of 37 °C. Then, the solution was kept continuously inside the water bath chamber until the water evaporated from the solution and residue remained. Subsequently, the residue paste was added with an excess of pure water (≈ 1 l) and vigorous stirring for 30 min at a temperature of 88 °C. Next, the resultant was added with 290 mL of DI water and then, slowly diluted the mixer using the 30% H_2O_2 with the continuous stirring. In the meantime, the obtained product turned to yellow from dark brown. The resultant precipitate was purified with 20% dilute HCl (100 ml) until the sulfate ions were removed from the precipitate and subsequently the brownish resultant product was allowed to precipitate down overnight. The same procedure was repeated until the brownish colour disappears and dispersion became neutral. Finally, the resultant dispersion was centrifuged and dried under vacuum condition inside the desiccator.

2.2.3. Reduction of GO

The synthesized 70 mg of GO was dissolved in 45 mL of pure water and then, the mixed solution was sonicated for 2 h. Further, 1 ml of ammonia was mixed to the dispersion solution to attain the pH of 9 and then, the resultant solution was shifted to a 50 ml of teflon coated autoclave. Next, the autoclave was kept in the hot furnace at a temperature of 160 °C for 24 h. After the process, the rGO was deposited as a black solid sample inside the autoclave. Finally, the resultant precipitate was purified using the pure water and wet under ambient condition.

2.3. Synthesis of MoWS2/rGO composites

180 mg of the $MoWS_2$ nanosheet was dispersed in a beaker with 60 mg of GO dispersion solution. Further, the solution was continuously stirred for 4 h to confirm the instinctive segregation of the positive charged $MoWS_2$ nanosheets with the negative charged GO sheets. Next, the resultant mixed solution shifted to a 50 mL teflon-coated autoclave and was kept in the hot furnace at a temperature of 130 °C for 32 h. After this process, the autoclave was cooled in the room temperature and then the precipitate was collected using centrifugation. Finally, the resultant dispersion was washed 3 times with ethanol-water mixture (2:1) and dried in ambient temperature overnight.

To further convert the $MoWS_2$@rGO composite solution into polymer com- posite thin film, the casting method using petri dish was applied. A little amount of the fabricated $MoWS_2$@rGO nanocomposite was mixed with PVA dispersed solution with an initial concentration of 15 mg ml^{-1} in the proportional volume ratio of 2:1. A resultant nanocomposite mixer was under the sonication process and then heated using the magnetic stirrer up to the temperature of 80 °C for 10 h on a hot plate until the sample precipitate to 1/3 of its initial content of solution. Then, the concentrated 1/3 solution was shifted into a small glass plate and wetted in a hot furnace for the duration of 12 h.

2.4. Characterization

The sample of layered $MoWS_2$ nanosheets and $MoWS_2$/rGO nanocomposite were analyzed with x-ray diffraction (XRD) using Bruker D8 Advance equipment. Figure 1 depicts the XRD spectra of the synthesized $MoWS_2$/rGO (indicates in red colour) and $MoWS_2$ (indicates in blue colour) sample. The $MoWS_2$ sample indicates the diffraction peaks at 13.91°, 59.01° and 33.49° along the planes of [0 0 1], [1 1 0] and [1 0 1], respectively and all the peaks matche well to the standard MoS_2 with hexagonal structure (JCPDS No.37- 1492) [32]. Besides, the fixed WS_2 and MoS_2 structures along the plane [0 0 2] possess the diffraction peaks at 14.32° and 14.38°, respectively. Further, the obtained peaks along the horizontal plane [0 0 2] for the synthesized sample of $MoWS_2$ are lower than the fixed terms, that infers the involvement of strain, stress and a huge interlayer spacing between the layers in the structure for the fabricated samples [33].

Subsequently, for the $MoWS_2$@rGO nanocomposite sample, all the observed diffraction peaks are broadened which indicates the decrease in degree of crystallinity, particle size and an increase of defect density which arises due to the active sites of the

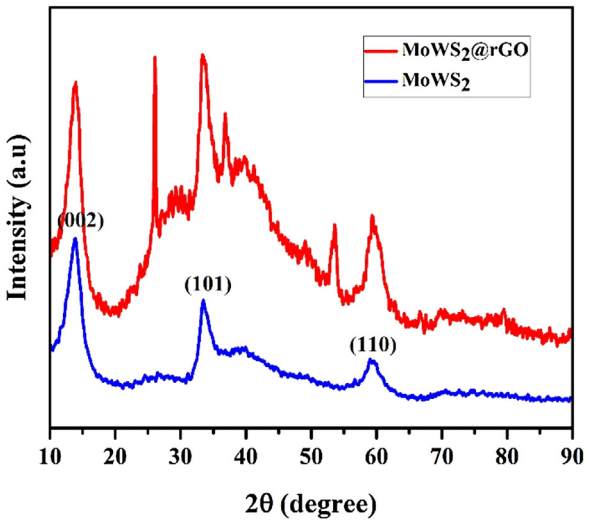

Fig. 1. XRD characterization of $MoWS_2$ and $MoWS_2$@rGO nanocomposite.

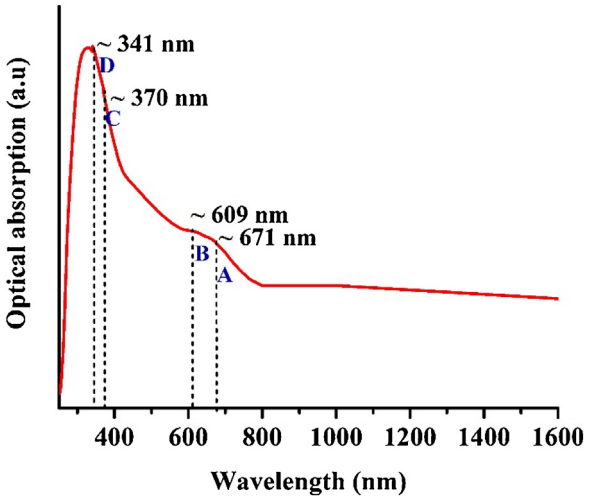

Fig. 2. Linear optical absorption analysis of synthesized nanocomposite.

nanocomposite sample. Further, the ultraviolet-visible (UV–vis) spectroscopy characterization was carried out by a spectrophotometer (200 –1600 nm of Wavelength) (JASCO- V670) and the result is depicted in Fig. 2. From the figure, four peaks are observed at 671 (A), 609 (B), 370 (C) and (D). The MoS_2 have standard A, B, C and D peaks at 665 (A), 605 (B), 440 (C) and 395 nm (D) [34]. After doping W between the Mo-S bonds, A, B peaks almost same and C, D peaks exhibit blue-shift due to the variation in the density of the characterized sample state region structure. Moreover, after the rGO composite with $MoWS_2$, the peaks are smoothened and absorption peaks look like soft curves.

Next, the high resolution-transmission electron microscopy (HR-TEM) characterizations were performed using a Tecnai, Twin electron microscope (G2 20). Figure 3 confirms the layered form of the synthesized nanocomposite and also infers the two different nanostructure which stack at different inter-layer widths of 0.341 nm, 0.673 nm for rGO and $MoWS_2$ respectively. Additionally, the steep edge in the image confirms the crystalline structure of the layered $MoWS_2$/rGO and indexes the hexagonal structure. Further, the elemental proposition of the synthesized nanocomposite sample was analyzed using the energy dispersive X-ray (EDX) and results are depicts in Fig. 3(b). These results confirm that the fabricated sample is the composite of W, Mo, C, O and S components.

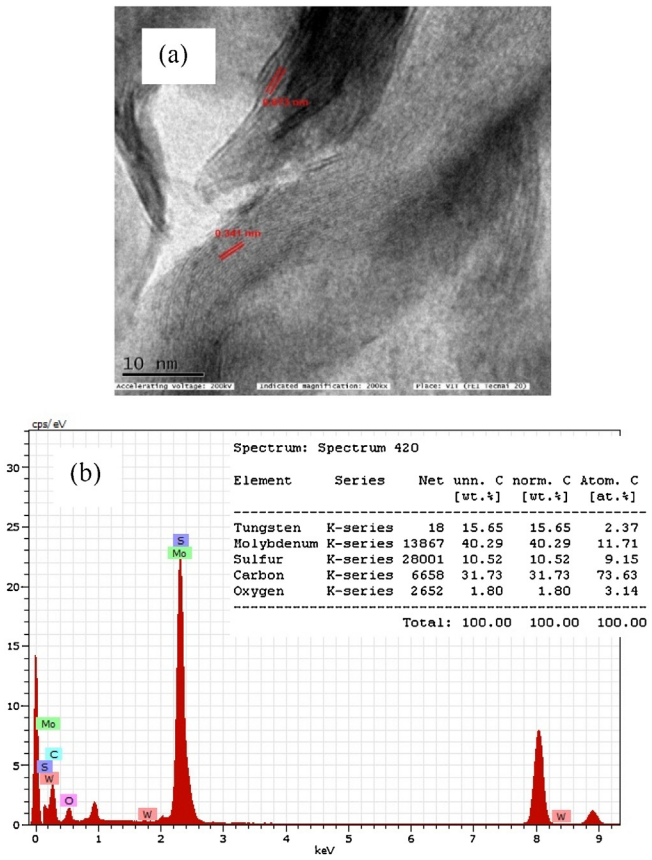

Fig. 3. (a) HR-TEM morphology picture of the layered $MoWS_2$/rGO sample (b) Component proposition of the fabricated nanocomposite.

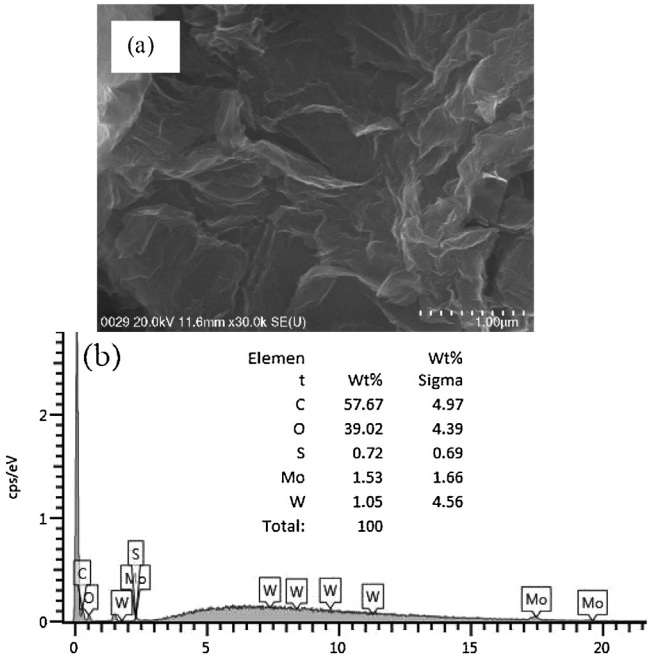

Fig. 4. (a) FE-SEM, morphology picture of the layered $MoWS_2$/rGO-PVA film, (b) Component proposition of the fabricated nanocomposite.

Further, to confirm the formation of $MoWS_2$/rGO nanocomposite the field emission-scanning electron microscopy (FE-SEM) analysis was executed using Hitachi (SU8220). Figure 4(a) depicts the morphology of the $MoWS_2$/rGO nanocomposite with the PVA

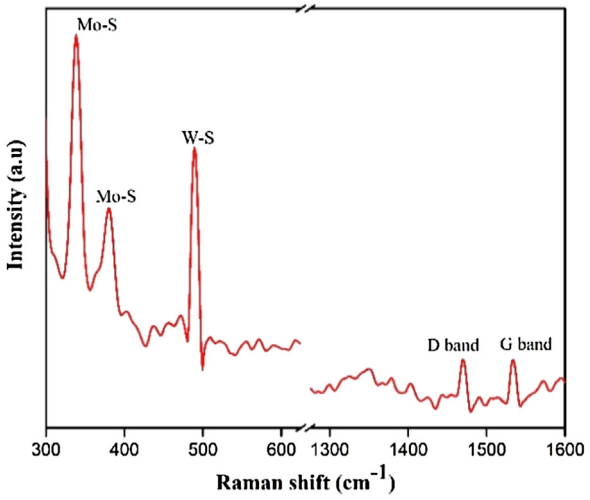

Fig. 5. Raman spectrum of $MoWS_2$/rGO nanocomposite.

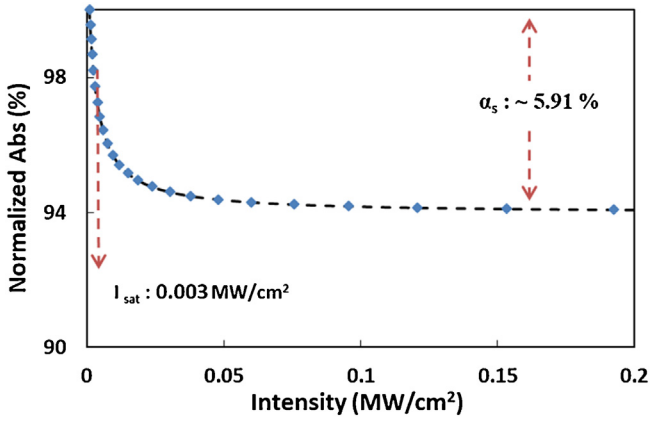

Fig. 6. Nonlinear absorption characterization of $MoWS_2$/rGO nanocomposite thin film.

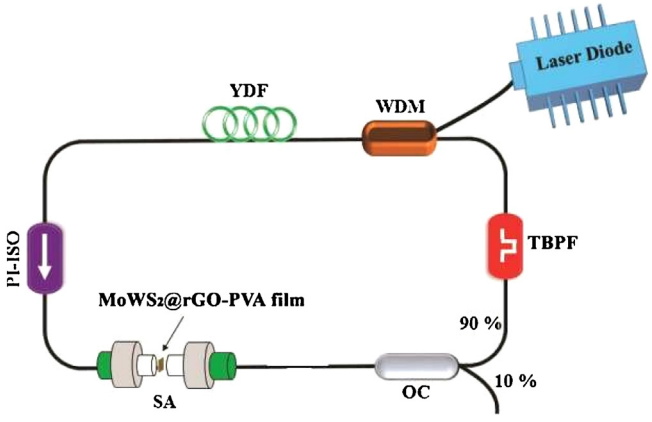

Fig. 7. Schematic representation of the proposed tunable Q-switched YDFL. Polarization insensitive isolator - PI-ISO, wavelength division multiplexer - WDM; tunable band pass filter - TBPF, output coupler - OC, ytterbium-doped fiber - YDF.

film. Further, the figure confirms the uniform distribution of layered $MoWS_2$ on the rGO nanosheets. Additionally, Figure 4(b) shows the elemental composition of W, Mo, C, O and S components in the PVA film of $MoWS_2$/rGO nanocomposite using the EDX characterization.

Furthermore, the Raman spectrum analysis was carried out on the synthesized sample $MoWS_2$/rGO composite using Renishaw inVial Raman spectroscopy with a wavelength of 532 nm. Figure 5

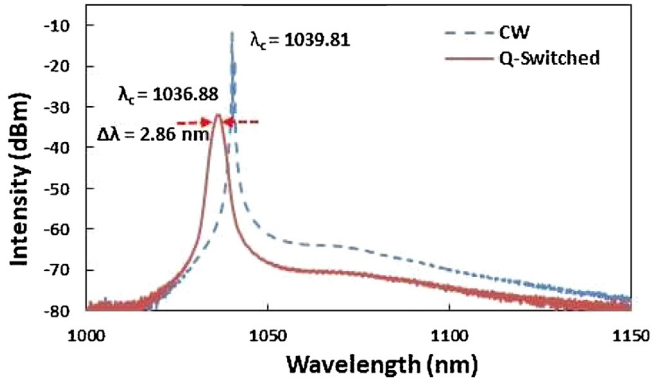

Fig. 8. Optical spectrum of the YDFL set up, presence and absence of $MoWS_2$/rGO-PVA SA.

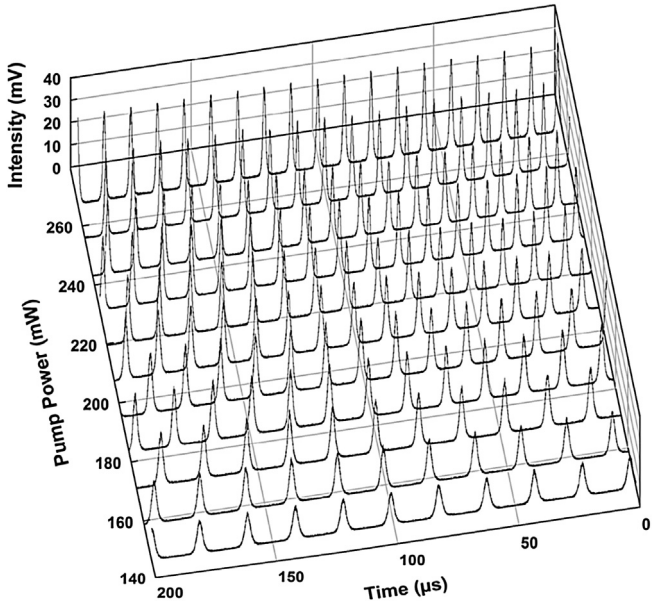

Fig. 9. 3-D pulse train progress inside the proposed YDFL for the pump power range from mW to 267.4 mW.

indicates the Raman spectrum with the peaks of 349.6 cm^{-1}, 391.3 cm^{-1}, 494.7 cm^{-1}, 1460 cm^{-1} and 1550 cm^{-1}. The first two peaks represent the E12 g and A1g modes, respectively. Generally, the standard Mo-S structure has the peaks at 407 and 374 cm^{-1} [35]. After W- atom doping and rGO composite, the peaks are shifted and the third peak observed at 494.7 cm^{-1} which indicates the presence of W—S structure. The formation of rGO component is confirmed by the two peaks each at 1550 cm^{-1} and 1460 cm^{-1} that corresponds to G and D band, respectively. These peaks confirm that the analyzed sample is the $MoWS_2$@rGO nanocomposite.

In addition to the characterization on material structure and chemistry, the nonlinear optical performance of the $MoWS_2$/rGO composite thin film has been investigated. This characterization was done by using a twin-detection technique which utilized a home-made laser operating at 1560 nm wavelength, 28.169 MHz pulse repetition rate and 2.33 ps pulse width as the seed laser. A variable attenuator with maximum attenuation of 60 dB is used to vary the incident intensity on the $MoWS_2$@rGO SA under characterization. From the result as shown in Fig. 6, the saturation intensity of the $MoWS_2$@rGO SA is of 0.003 MW/cm^2 whereas the modulation depth is 5.91%.

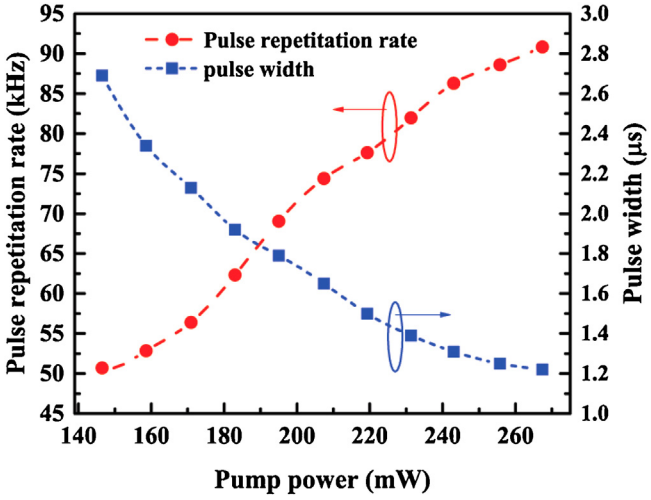

Fig. 10. Evolution of pulse width and pulse repetition rate of the YDFL for the pumped power range from 146.7 mW to 267.4 mW.

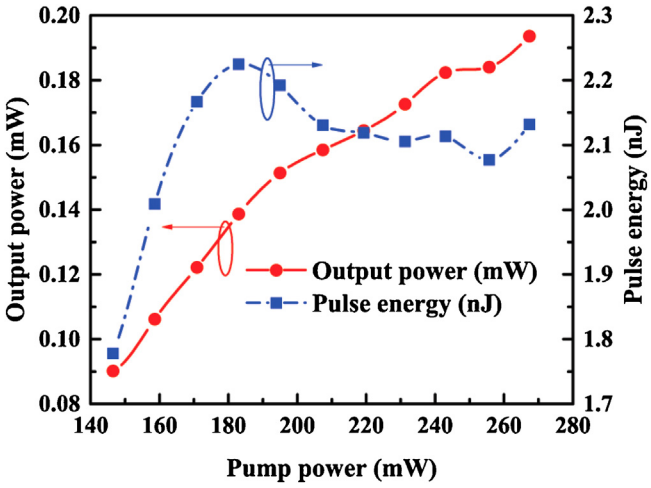

Fig. 11. Evolution of pulse energy and output power of the proposed YDFL for the induced power range from 146.7 mW to 267.4 mW.

3. Experimental setup

The diagrammatic representation of the $MoWS_2$/rGO-PVA SA based tunable YDFL cavity is depicted in Fig. 7. The laser diode at a 980 nm wavelength (LU0975M500) is spliced into the 980 nm wavelength port of the wavelength division multiplexer 980/1064 nm (WDM) to pump the gain media.

The 70 cm length of the Yb-doped gain fiber (1330 dB/m absorption at 977 nm, mode field diameter = 5.1 μm, NA = 0.17) acts as the gain medium. Another end of the Yb-doped gain fiber is connected with the polarization independent optical isolator which guarantees an unidirectional optical propagation inside the laser cavity. After isolator, the fabricated thin film SA is sandwiched between the fiber ferrules which act as the SA. The fabricated SA helps in the generation of Q-switched laser pulse inside the cavity. Thus, the generated pulse is tapped through a 90:10 output coupler and as the standard configuration, 90% of the light feeds into the cavity. Further, the fiber based tunable bandpass filter (Agiltron) with a tuning resolution of 0.01 nm is incorporated between the optical coupler and WDM to analyse the tuning property of the laser cavity.

The tapped 10% of output is analyzed in the optical domain, time domain and frequency domain using optical spectrum analyzer (Yokogawa, AQ6370B), oscilloscope (Yokogawa, DLM2054, 2.5GS/s-500 MHz), and radio frequency (RF) spectrum analyzer (Anritsu, MS2683 A), respectively. Optical powers are measured using optical power meter (Thorlabs, PM100USB).

4. Result and discussions

In this YDFL cavity, without incorporating SA, the continuous wave (CW) emission occurs during the injection of pump power. After incorporating the fabricated SA, the Q-switched pulses are observed at the threshold power of 146.7 mW. Further, the generated pulse is stable up to the highest induced power threshold of 267.4 mW. Furthermore, the generated laser pulse wavelength range possess a firm spatial spectrum, a significant broadening because of self-phase modulation effect (SPM) and a wavelength shift because of the loss induced by the SA. Subsequently, Figure 8 clearly shows the spectrum of CW at the centre wavelength of 1039.81 nm with full- width half maximum (FWHM) of ~ 0.01 nm and the generated pulse operating at the centre wavelength of 1036.88 nm along with FWHM of 2.86 nm.

Figure 9 shows the 3-D pulse progress in the YDFL cavity throughout the Q-switching operation for the pump power range

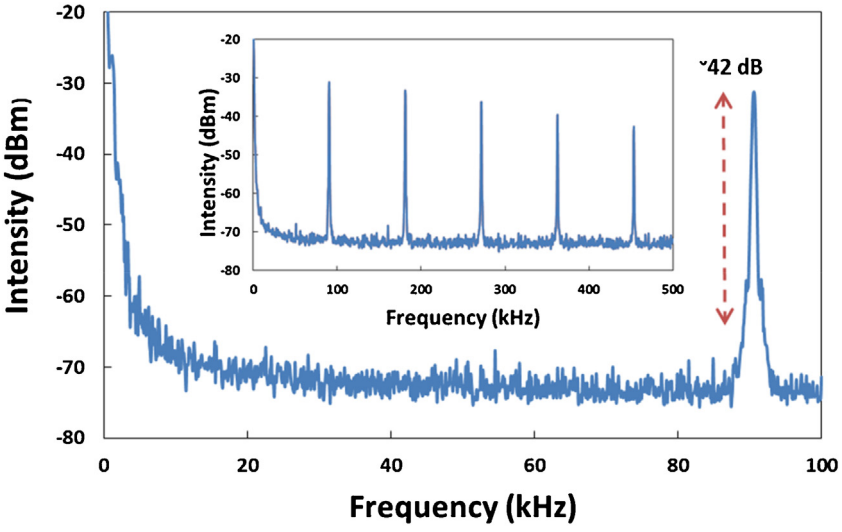

Fig. 12. RF spectrum of the proposed YDFL at the highest pumped power of 267.4 mW.

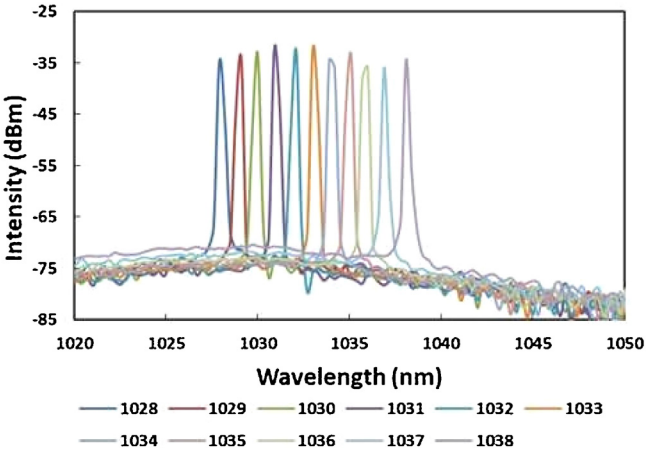

Fig. 13. Optical spectrum of the generated pulses with tunable wavelength for a highest pumped power of 267.4 mW.

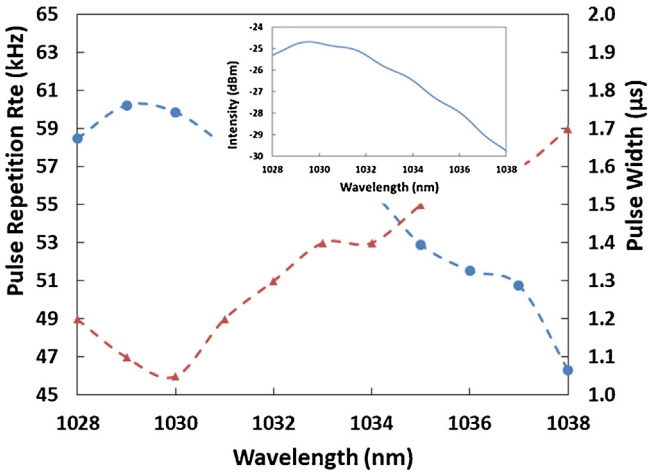

Fig. 14. Pulse width and pulse repetition rate characteristics of the YDFL at the highest pumped power of 267.4 mW.

of 146.7 mW–267.4 mW. For these pump power, stable pulses are realized. Additionally, as pump power increases, the Q-switched pulses follows the trend of increasing repetition rate, a decreasing pulse width and an increasing pulse intensity. This variation obeys with the theory of Q-switching mechanism.

Figure 10 depicts the brief analysis for the pulse width and pulse repetition rate of the generated pulse train throughout the Q-switched operating power range. When the pumped power increased from 146.7 mW to 267.4 mW inside the laser cavity, the pulse repetition rate rises from 50.70 kHz to 90.84 kHz and the pulse width reduces from 2.69 μs to 1.22 μs. The rising trend of pulse repetition rate is because of the fast saturation time in both the SA, as well as laser gain medium at maximum pump power. Subsequently, the decreasing trend in pulse width is due to the reduction in discharge and charge time in the laser cavity.

Figure 11 represents the detailed analysis of the pulse energy and output power of the generated pulse train for the complete Q-switched operating power range. When the pumped power varies from 146.7 mW to 267.4 mW, the output aver- age power rises from 0.09 mW to 0.193 mW, at the same time the pulse energy also rises from 1.77 nJ to 2.13 nJ. Beyond the induced power of 183 mW, a slow degradation in the Q-switch behaviour has been noted in the pulse energy because of the decrease in the ratio between output power and pulse repetition rate at maximum induced powers.

Further, the stable characteristics of the proposed YDFL pulsed laser is analyzed by measuring its RF spectrum at highest induced power of 267.4 mW which is depicted in Fig. 12. From the figure, it is understood that the proposed laser cavity have the fundamental frequency (FF) of ~ 90.7 kHz with an extinction ratio of ~ 42 dB. Further, the insets of Fig. 12 depicts the decreasing trend in the amplitude of the frequency components which are multiples of fundamental frequency, this confirms the stable nature of the pulses generated in the YDFL cavity.

Besides, the tunable characteristics of the proposed YDFL is also investigated by manual tuning of TBPF which is incorporated inside the cavity. Figure 13 depicts the spectrum of the tunable wavelengths for the generated Q-switched pulses at a highest induced power of 267.4 mW. Further, the figure shows the Q-switched tunable stable pulses that are observed from the wavelength of 1028 nm to 1038 nm. Additionally, this tuning wavelength range confirms that the proposed $MoWS_2$/rGO-PVA SA possess the potential to generate the tunable pulses in YDFL with a tunable bandwidth of ~ 10 nm.

Figure 14 shows the characteristics analysis of the pulse width and pulse repetition rate of the tunable YDFL over the operating tunable wavelength range. Further, the figure confirms that the progress pattern of the pulse width and pulse repetition rate of the YDFL matches well with the gain medium profile of the YDFL. This is represented as the spontaneous emission spectrum of the YDFL in the inset of Fig. 13. This matching confirms the change in repetition rate and power dependent on the gain profile. Additionally, this correlation confirms the stability of the proposed YDFL cavity. The comparison on the output performance of Q-switched laser generated using different SA is shown in Table 1.

5. Conclusions

In this proposed work, the nanocomposite of $Mo_{(1-x)}W_xS_2$@rGO-PVA based SA has been fabricated using the x composition of 0.2. The fabricated SA exhibits an improved photo-response and a good optical absorption that results in the generation of the tunable Q-switched laser for the wavelength range of 1028–1038 nm. Subsequently, at the maximum induced power of 267.4 mW, the achieved highest pulse repetition rate and narrowest pulse width are 90.84 kHz and 1.22 μs, respectively. This demonstration confirms that the $MoWS_2$@rGO-PVA nanocomposite will act as the potential SA for the realization of an all-fiber tunable Q-switched ytterbium-doped laser.

Author statement

In the recent times, two-dimensional nanomaterials are highly focused in the development of pulsed lasers owing to its unique

Table 1
Comparison on the output performance of YDF Q- switched laser generated using different 2D SAs.

Saturable Absorber	Operating wavelength (nm)	Operating Power (mW)	Pulse Repetition Rate (kHz)	Pulse Width (μs)	Reference
Black phosphorus/ PVA	1056	129.4–231.6	6.0–44.8	5.6-4	[36]
MoS_2/PVA	1030	0.1–0.9	5.8–17.9	26.7–3.3	[37]
WS_2/PVA	1036	0.13–0.53	24.9–36.7	6.4–3.2	[38]
Graphene/PVA	1030	50–170	25–135	4.5–1.35	[39]
$MoWS_2$-rGO/PVA	1039	0.09–1.93	50.7–90.8	2.66–1.22	This Work

characteristics. In particular, graphene and its derivatives such as transition metal dichalcogenides (TMDs) have been widely reported in photonic based applications. In specific, TMDs have distinctive properties compared to graphene such as switchable bandgaps and photoluminescence. Currently, the advances in chemical synthesis process pay the way for the exploration of alloying TMDs for ultra-pulse generation. In this paper, a saturable absorber made up of nanocomposite rGO-$MoWS_2$ has been fabricated and incorporated into a Yb-doped fiber laser (YDFL) cavity operating at 1 μm wavelength. An all-fiber tunable YDFL laser based on $MoWS_2$@rGO/PVA-SA generates stable Q-switched pulses with a central wavelength of 1036.88 nm with FWHM of ~ 2.86 nm and a tunable operating range from 1028 nm to 1038 nm. For the operating pump power range from 146.7 mW to 267.4 mW, the generated Q-switched pulse exhibits the pulse width from 2.69 μs to 1.22 μs, a pulse repetition rate from 50.70 kHz to 90.84 kHz, an output power from 0.09 mW to 0.193 mW, and a pulse energy from 1.77 nJ to 2.13 nJ. To the best of our knowledge, this is the first demonstration of a tunable Q-switched YDFL using the $MoWS_2$@rGO nanocomposite saturable absorber.

Acknowledgements

S. Sivabalan wishes to thank DST (no. EMR/2016/003410), the government of India, for the financial support through the project. The authors gratefully acknowledge VIT, Vellore for the support through Seed Grant for Research.

References

[1] A. Hideur, T. Chartier, C.O.żkul, F. Sanchez, All-fiber tunable ytterbium- doped double-clad fiber ring laser, Opt. Lett. 26 (14) (2001) 1054–1056.
[2] H. Wu, J. Wu, Q. Yu, K. Zhang, H. Xiao, J. Leng, J. Xu, P. Zhou, Over 70nm broadband-tunable yb-doped fiber pulse laser based on trilaminar graphene, Laser Phys. Lett. 14 (6) (2017), 065105.
[3] H. Ahmad, M.A.M. Salim, S.R. Azzuhri, M.R.K. Soltanian, S.W. Harun, A passively q-switched ytterbium-doped fiber laser based on a few- layer bi_2se_3 saturable absorber, Laser Phys. 25 (6) (2015), 065102.
[4] J. Mohanraj, V. Velmurugan, S. Sivabalan, Transition metal dichalco- genides based saturable absorbers for pulsed laser technology, Opt. Mater. 60 (Supplement C) (2016) 601–617.
[5] N. Xu, W. Yang, H. Zhang, Nonlinear saturable absorption properties of indium selenide and its application for demonstrating a Yb-doped mode-locked fiber laser, Opt. Mater. Express 8 (2018) 3092–3103.
[6] Z. Sun, T. Hasan, F. Torrisi, D. Popa, G. Privitera, F. Wang, F. Bonac- corso, D.M. Basko, A.C. Ferrari, Graphene mode-locked ultrafast laser, ACS Nano 4 (2) (2010) 803–810.
[7] A.K. Geim, K.S. Novoselov, The rise of graphene, Nat. Mater. 6 (2007) 183–191.
[8] Q. Bao, K.P. Loh, Graphene photonics, plasmonics, and broadband optoelectronic devices, ACS Nano 6 (5) (2012) 3677–3694.
[9] A. Martinez, Z. Sun, Nanotube and graphene saturable absorbers for fibre lasers, Nat. Photon. 7 (2013) 842–845.
[10] Y. Chen, G. Jiang, S. Chen, Z. Guo, X. Yu, C. Zhao, H. Zhang, Q. Bao, S. Wen, D. Tang, D. Fan, Mechanically exfoliated black phosphorus as new saturable absorber for both q-switching and mode-locking laser operation, Opt. Express 23 (10) (2015) 12823–12833.
[11] K. Wang, J. Wang, J. Fan, M. Lotya, A. ONeill, D. Fox, Y. Feng, X. Zhang, B. Jiang, Q. Zhao, H. Zhang, J.N. Coleman, L. Zhang, W.J. Blau, Ultra- fast saturable absorption of two-dimensional mos_2 nanosheets, ACS Nano 7 (10) (2013) 9260–9267.
[12] Z. Li, Y. Zhang, Ch. Cheng, H. Yu, F. Chen, 6.5 GHz Q-switched mode-locked waveguide lasers based on two-dimensional materials as saturable absorbers, Opt. Express 26 (2018) 11321–11330.
[13] K. Niu, Q. Chen, R. Sun, B. Man, H. Zhang, Passively Q-switched erbium-doped fiber laser based on SnS2 saturable absorber, Opt. Mater. Express 7 (2017) 3934–3943.
[14] K. Niu, R. Sun, Q. Chen, B. Man, H. Zhang, Passively mode-locked Er-doped fiber laser based on SnS2 nanosheets as a saturable absorber, Photon. Res. 6 (2018) 72–76.
[15] L. Ziqi, D. Ningning, Z. Yuxia, W. Jun, Y. Haohai, Ch. Feng, Invited article: mode-locked waveguide lasers modulated by rhenium diselenide as a new saturable absorber, APL Photon. 3 (2018) 080805.
[16] L. Sun, Z. Lin, J. Peng, J. Weng, Y. Huang, Z. Luo, Preparation of few- layer bismuth selenide by liquid-phase-exfoliation and its optical absorption properties, Sci. Rep. 4 (2014) 4794.
[17] P. Tonndorf, R. Schmidt, P. Böttger, X. Zhang, J. Börner, A. Liebig, M. Albrecht, C. Kloc, O. Gordan, D.R.T. Zahn, S.M. de Vasconcellos, R. Bratschitsch, Photoluminescence emission and raman response of monolayer mos_2, $mose_2$, and wse_2, Opt. Express 21 (4) (2013) 4908–4916.
[18] H.S. Shin, G. Eda, L.-J. Li, K.P. Loh, H. Zhang, The chemistry of two- dimensional layered transition metal dichalcogenide nanosheets, Nat. Chem. 5 (2013) 263–275.
[19] X. Zhang, S. Zhang, C. Chang, Y. Feng, Y. Li, N. Dong, K. Wang, L. Zhang, W.J. Blau, J. Wang, Facile fabrication of wafer-scale mos_2 neat films with enhanced third-order nonlinear optical performance, Nanoscale 7 (2015) 2978–2986.
[20] P.D. Tran, S.Y. Chiam, P.P. Boix, Y. Ren, S.S. Pramana, J. Fize, V. Artero, J. Barber, Novel cobalt/nickel-tungsten-sulfide catalysts for electro catalytic hydrogen generation from water, Energy Environ. Sci. 6 (2013) 2452–2459.
[21] Y. Chen, J. Xi, D.O. Dumcenco, Z. Liu, K. Suenaga, D. Wang, Z. Shuai, Y.-S. Huang, L. Xie, Tunable band gap photoluminescence from atomically thin transition-metal dichalcogenide alloys, ACS Nano 7 (5) (2013) 4610–4616.
[22] S.D. Karande, N. Kaushik, D.S. Narang, D. Late, S. Lodha, Thickness tunable transport in alloyed wsse field effect transistors, Appl. Phys. Lett. 109 (14) (2016) 142101.
[23] V. Kiran, D. Mukherjee, R.N. Jenjeti, S. Sampath, Active guests in the mos_2/$mose_2$ host lattice: efficient hydrogen evolution using few-layer al- loys of mos_2(1-x)se_2x, Nanoscale 6 (2014) 12856–12863.
[24] L.M. Xie, Two-dimensional transition metal dichalcogenide alloys: preparation, characterization and applications, Nanoscale 7 (2015) 18392–18401.
[25] H. Li, K. Yu, Z. Tang, Z. Zhu, Experimental and first-principles investigation of $mows_2$ with high hydrogen evolution performance, ACS Appl. Mater. Interfaces 8 (43) (2016) 29442–29451.
[26] D. Chen, W. Chen, L. Ma, G. Ji, K. Chang, J.Y. Lee, Graphene-like layered metal dichalcogenide/graphene composites: synthesis and applications in energy storage and conversion, Mater. Today 17 (2014) 184–193.
[27] Q. Liu, J. Tian, W. Cui, P. Jiang, N. Cheng, A.M. Asiri, X. Sun, Carbon nanotubes decorated with cop nanocrystals: a highly active non-noble- metal nanohybrid electrocatalyst for hydrogen evolution, Angew. Chem. Int. Ed. 53 (2014) 6710–6714.
[28] H. Mu, Z. Wang, J. Yuan, S. Xiao, C. Chen, Y. Chen, Y. Chen, J. Song, Y. Wang, Y. Xue, H. Zhang, Q. Bao, Graphene/bi2te_3 heterostructure as saturable absorber for short pulse generation, ACS Photonics 2 (2015) 832–841.
[29] Z. Li, C. Cheng, N. Dong, C. Romero, Q. Lu, J. Wang, J.R.V. de Aldana, Y. Tan, F. Chen, Q-switching of waveguide lasers based on graphene/ws_2 van der waals heterostructure, Photon. Res. 5 (2017) 406–410.
[30] W.S. Hummers, R.E. Offeman, Preparation of graphitic oxide, J. Am. Chem. Soc. 80 (1958) 1339.
[31] M. Hirata, T. Gotou, S. Horiuchi, M. Fujiwara, M. Ohba, Thin-film particles of graphite oxide 1:2: high-yield synthesis and flexibility of the particles, Carbon 42 (2004) 2929–2937.
[32] F. Li, J. Li, Z. Cao, X. Lin, X. Li, Y. Fang, X. An, Y. Fu, J. Jin, R. Li, Mos2 quantum dot decorated rgo: a designed electrocatalyst with high active site density for the hydrogen evolution reaction, J. Mater. Chem. A 3 (2015) 21772–21778.
[33] Z. Luo, Y. Huang, M. Zhong, Y. Li, J. Wu, B. Xu, H. Xu, Z. Cai, J. Peng, J. Weng, 1-, 1.5-, and 2- μm fiber lasers q-switched by a broadband few- layer mos_2 saturable absorber, J. Lightwave Technol. 32 (2014) 4679–4686.
[34] M. Zhang, R.C.T. Howe, R.I. Woodward, E.J.R. Kelleher, F. Tor- risi, G. Hu, S.V. Popov, J.R. Taylor, T. Hasan, Solution processed mos_2-pva composite for sub-bandgap mode-locking of a wideband tunable ultrafast er:fiber laser, Nano Res. 8 (2015) 1522–1534.
[35] X. Wang, H. Feng, Y. Wu, L. Jiao, Controlled synthesis of highly crystalline mos_2 flakes by chemical vapor deposition, J. Am. Chem. Soc. 135 (2013) 5304–5307.
[36] H. Ahmad, M.A.M. Salim, K. Thambiratnam, S.F. Norizan, S. Harun, A black phosphorus-based tunable Q-switched ytterbium fiber laser, Laser Phys. Lett. 13 (2016), 095103.
[37] Z. Luo, Y. Huang, M. Zhong, Y. Li, J. Wu, B. Xu, H. Xu, Z. Cai, J. Peng, J. Weng, 1-, 1.5-, and 2 μm fiber lasers q-switched by a broadband few-layer mos2 saturable absorber, J. Lightwave Technol. 32 (2014) 4077–4084.
[38] M. Zhang, G. Hu, R. Howe, L. Chen, Z. Zheng, T. Hasan, Yb-and er-doped fiber laser Q-switched with an optically uniform, broadband ws 2 saturable absorber, Sci. Rep. 5 (2015), srep17482.
[39] L. Hou, J. Sun, H. Guo, Q. Lin, Y. Wang, Y. Bai, L. Baole, H. Chen, J. Bai, High-efficiency, high-energy ytterbium-doped Q-switched fibre laser with graphene oxide-COOH saturable absorber, Laser Phys. Lett. 15 (2018), 075103.